MATERIALS CHEMISTRY
FRONTIERS

RESEARCH ARTICLE

View Article Online
View Journal | View Issue

Cite this: *Mater. Chem. Front.*, 2021, **5**, 6092

Regulating the adsorption behavior of intermediates on Ir–W@Ir–WO_{3-x} boosts acidic water oxidation electrocatalysis†

Zheng Lu,‡ Cong Wei,‡ Xinmiao Liu, Yanyan Fang, Xiaobin Hao, Yipeng Zang, Zhibin Pei, Jinyan Cai, Yishang Wu, Di Niu, Amirabbas Mosallanezhad, Da Sun, Jian Ye, Shuwen Niu* and Gongming Wang *

Received 9th April 2021,
Accepted 9th June 2021

DOI: 10.1039/d1qm00551k

rsc.li/frontiers-materials

Tungsten oxide with strong acid resistance and weak O-binding ability could potentially achieve a tradeoff on the O-binding properties by constructing W and Ir dual sites for acidic oxygen evolution reaction (OER) catalysis. However, the peroxide intermediate formed during the OER process could react with tungsten oxide to produce soluble species, thereby severely limiting its application. Herein, we construct Ir–W@Ir–WO_{3-x} core–shell nanoparticles with an Ir–W metallic core and an Ir-doped WO_{3-x} (Ir–WO_{3-x}) shell, which can deliver an impressive overpotential of 261 mV at 10 mA cm^{-2} for acidic OER catalysis and extraordinary catalytic stability. Spectroscopic analysis manifests that Ir–W@Ir–WO_{3-x} could substantially suppress peroxide species formation and effectively avoid peroxide-induced corrosion during the OER process. Theoretical studies reveal that the moderate O-binding capability on Ir–W@Ir–WO_{3-x} not only accelerates catalytic kinetics, but also restrains hydroperoxide formation. This work sheds light on the rational design of OER catalysts by modulating the adsorption behavior of oxygen-containing intermediates.

Introduction

Among all the solutions to solve the ever-growing global energy consumption and the consequent environmental issues, developing a clean hydrogen fuel to replace conventional fossil fuel is one of the most promising pathways toward constructing a renewable and carbon-neutral energy system.[1,2] Water electrolysis using a proton exchange membrane (PEM) system has been regarded as an attractive electrolysis technology due to its high energy efficiency, compact design and fast load change capability.[3] However, the proton transported PEM electrolysis is typically operated in a highly acidic environment, which consequently leads to severe corrosion issues.[4] Most of the non-noble catalysts used in PEM electrolysis, especially oxygen evolution reaction (OER) catalysts, cannot well survive under this corrosive conditions.[4–8] Although a great number of OER catalysts with excellent catalytic activities have been developed for alkaline electrolysis, hardly any of them can be readily operated in an acidic environment.[9–21] Moreover, with the rapid development of PEM electrolysis, unveiling the underlying instability mechanism and constructing highly stable yet efficient acidic OER catalysts are extremely important and attract immense attention.

Among the ever-reported acidic OER catalysts, IrO_2 with superior anti-dissolution feature has been considered as a great candidate for PEM application.[22–24] Unfortunately, the high price induced by the natural scarcity of Ir in the earth's crust limits its large-scale application.[25] Additionally, the strong binding affinity toward oxygen intermediates could essentially limit the formation of OOH* on the surface of IrO_2 based on the ever-reported volcano plots, which basically results in unsatisfactory activity for OER catalysis.[26,27] In this regard, manipulating the Ir–O interactions to boost the intrinsic activity and also minimize the Ir contents is the most feasible strategy to develop highly efficient and affordable Ir-based catalysts for OER. Considering that carbon typically suffers from severe oxidative corrosion during the acidic OER process, employing metal oxides as the support matrix for IrO_x species to reduce Ir dosage and simultaneously tune the local electronic structure of the Ir sites to reasonably weaken the oxygen-binding ability has been explored for acidic OER catalysis.[22,23,27–35] For example, Seitz *et al.* found that the *in situ* generated amorphous IrO_x on $SrIrO_3$ surface can significantly enhance the OER performance of $SrIrO_3$ due to the optimized O-binding ability of the Ir sites.[23] Additionally, Yang *et al.* demonstrated that 6H-$SrIrO_3$ exhibited

Hefei National Laboratory for Physical Science at the Microscale, Department of Chemistry, University of Science and Technology of China, Hefei 230026, Anhui, China. E-mail: niusw@mail.ustc.edu.cn, wanggm@ustc.edu.cn

† Electronic supplementary information (ESI) available: Experimental section and ESI figures. See DOI: 10.1039/d1qm00551k

‡ These authors contributed equally to this work.

much higher activity and stability than 3C-$SrIrO_3$ and IrO_2 toward acidic OER catalysis. The superior activity and stability of 6H-$SrIrO_3$ originate from the weakened surface Ir–O binding ability induced by the existence of unique face-sharing IrO_6 dimers.[33] Moreover, Nong *et al.* constructed $IrNiO_x$ core–shell particles for acidic OER catalysis and achieved an enhanced activity. Nickel leaching during the OER process endows the adjacent oxygen more electrophilic properties thus facilitating the O–O bond formation.[32] However, acid-induced metal (Sr, Ni, and Ir) leaching is still obvious, and the long-term stability for acidic OER catalysis remains challenging.[27]

According to the volcano maps for OER catalysis,[26,27] tungsten oxide has a relatively weaker O-binding ability than IrO_2, which could potentially reach a tradeoff on the O-binding behavior by constructing W and Ir dual sites on a single catalyst surface. Moreover, tungsten oxides with strong anti-corrosion properties, cannot react with any inorganic acids apart from HF, which enables tungsten oxide to be an attractive candidate to anchor Ir sites for acidic OER catalysis. However, the biggest issue is the peroxide species,[36] the reaction intermediates formed during the OER process, which can react with tungsten oxide and produce a soluble peroxo-tungstate complex.[37–39] This is the reason why tungsten oxide is rarely used for acidic OER catalysis, despite having such excellent acidic resistance. To this end, manipulating the adsorption behavior of the crucial reaction intermediates to avoid the formation of peroxide species is the key to solving the solubility issues of tungsten oxide,[40] as shown in Scheme 1. Since surface adsorption properties are essentially determined by the local electronic structure of the adsorption sites, rationally constructing superior catalytic sites on tungsten oxides could fundamentally address the peroxide-induced solubility issues, but still remains unexplored.

Herein, we construct Ir–W@Ir–WO_{3-x} core–shell nanoparticles with a Ir–W metallic core and a Ir-doped WO_{3-x} (Ir–WO_{3-x}) shell by thermally reducing Ir-doped WO_3 (Ir–WO_3) under hydrogen atmosphere. The prepared Ir–W@Ir–WO_{3-x} exhibited an impressive overpotential of 261 mV at a current density of 10 mA cm^{-2} for acidic OER catalysis and extraordinary catalytic stability with only 3.5% potential increase in a constant 20 h chronopotentiometric test, which outperform most of the ever-reported acidic OER catalysts. Spectroscopic analysis demonstrates that the peroxide species and metal dissolution can be substantially suppressed with Ir–W@Ir–WO_{3-x} as the OER catalyst. Moreover, theoretical calculation reveals that the unique core–shell structures with moderate adsorption strength toward oxygen-containing intermediates not only accelerate the oxygen evolution reaction but also restrain the formation of hydroperoxide, which thus enable the superior catalytic activity and stability for acidic OER catalysis. The capability to regulate the surface adsorption behavior of the reaction intermediates paves a pathway toward the development of highly efficient and stable OER catalysts.

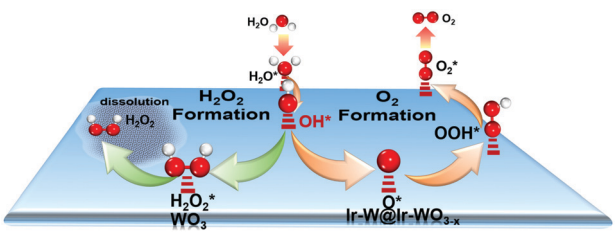

Scheme 1 Illustration of the strategy to suppress the formation of hydroperoxide by tuning the adsorption behavior of the reaction intermediates.

Results and discussion

Ir–W@Ir–WO_{3-x} nanoparticles (NPs) were synthesized *via* a typical two-step process. First, the Ir–WO_3 nanowires (NWs) were prepared through a modified hydrothermal reaction.[41] Then, the prepared Ir–WO_3 NWs were further reduced to Ir–W@Ir–WO_{3-x} NPs *via* high temperature reduction treatment under the temperature of 700 °C in a reducing atmosphere (details in the Experimental section, ESI†). Scanning electron microscopy (SEM) and transmission electron microscopy (TEM) characterization (Fig. 1a and Fig. S1, S2, ESI†) indicate the initial nanowire morphology of Ir–WO_3 changed to nanoparticle after a high temperature reduction treatment. The average size of the nanoparticles is around 200 nm. X-ray diffraction (XRD) was further performed to characterize the phase structure of the prepared samples. The initial Ir–WO_3 exhibits the typical characteristic peaks of the hexagonal WO_3 (JCPDS card no. 01-085-2459) and iridium doping does not change the intrinsic phase structure of WO_3 (Fig. 1b). Moreover, the XRD patterns (Fig. S3, ESI†) of Ir–WO_3 NWs do not match with the IrO_2 patterns and the high resolution transmission electron microscopy (HRTEM) images (Fig. S4, ESI†) further eliminated the formation of iridium oxide in Ir–WO_3 NWs. After a high temperature reduction treatment, all the diffraction peaks of the Ir–WO_3 disappear, and new peaks belonging to the metallic W (JCPDS card no. 01-089-3659) emerge. Inductively coupled plasma-atomic emission spectroscopy (ICP-AES) analysis indicates that the atomic ratio of Ir to W is around 6.7 at%. Furthermore, HRTEM images (Fig. 1c) and selected area electron diffraction[42] (SAED, selected region: blue square) pattern (Fig. 1d) reveal that the nanoparticle exhibits a tungsten core and an amorphous shell with a thickness of around 5 nm. Meanwhile, the high-angle annular dark-field scanning transmission electron microscopy (HAADF-STEM) and the corresponding energy dispersive spectroscopy (EDX) line scan and mapping images of Ir–W@Ir–WO_{3-x} were conducted to probe the elemental distribution over a single nanoparticle (Fig. 1e and f). The EDX profiles reveal that the signal of oxygen is mainly located at the shell, while the Ir and W elements are homogenously distributed over the whole nanoparticle. Therefore, the amorphous shell is expected to be tungsten oxides with Ir as the dopant.

To probe the chemical states of Ir–W@Ir–WO_{3-x}, Raman spectroscopy and X-ray photoelectron spectroscopy (XPS) were further performed. The Raman profiles of the pristine WO_3, Ir–WO_3 and Ir–W@Ir–WO_{3-x} are shown in Fig. S5 (ESI†). Both Ir–WO_3 and Ir–W@Ir–WO_{3-x} display the same characteristic

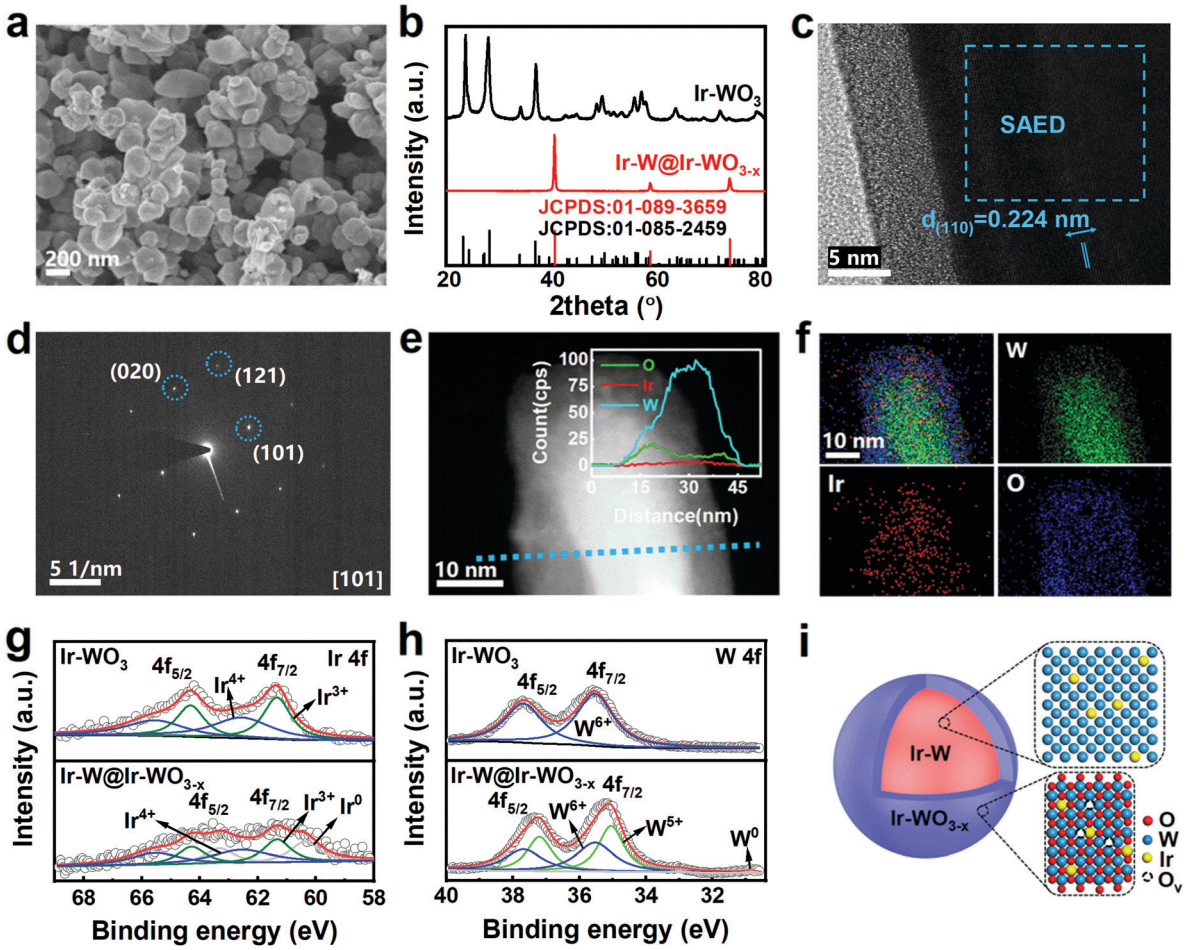

Fig. 1 (a) SEM image of Ir–W@Ir–WO_{3-x} NPs. (b) XRD patterns of Ir–W@Ir–WO_{3-x} NPs and Ir–WO_3 NWs. (c) The HRTEM image of Ir–W@Ir–WO_{3-x} NPs. (d) The SAED pattern of the highlighted area in (c) with the zone axis of [101]. (e) The HAADF-STEM image with the EDX line-scanning profiles (inset) of Ir, W and O and (f) the corresponding element mapping images over Ir–W@Ir–WO_{3-x} NPs. XPS core-level spectra of (g) Ir 4f and (h) W 4f spectra of Ir–W@Ir–WO_{3-x} and Ir–WO_3, respectively. (i) The schematic illustration of the core–shell structure of Ir–W@Ir–WO_{3-x}.

peaks with WO_3, suggesting that the surface of the Ir–W@Ir–WO_{3-x} nanoparticles are covered with tungsten oxides.[43] Besides, the electronic structures were examined by high resolution XPS. Fig. 1g shows the core-level XPS Ir 4f spectra of Ir–WO_3 and Ir–W@Ir–WO_{3-x}. XPS fitting analysis reveal that Ir in Ir–WO_3 is mainly in the oxidation state (Ir^{3+}, 61.34 eV; Ir^{4+}, 62.56 eV),[29,44] while Ir–W@Ir–WO_{3-x} exhibit one more metallic state (Ir^0, 60.38 eV).[44] The metallic signal might originate from the metallic core, because the detection depth of XPS is greater than the thickness of the oxide shell in some regions. Meanwhile, the W 4f XPS spectra (Fig. 1h) show that the binding energy of Ir–W@Ir–WO_{3-x} displays an obvious negative shift in comparison with that of Ir–WO_3. The shift is attributed to the existence of abundant lower oxidation state of tungsten (W^{5+}),[45] suggesting the formation of large amount of oxygen vacancies in the amorphous shell. Furthermore, the O 1s XPS spectra (Fig. S6, ESI†) also prove the existence of oxygen vacancies.[46] Taken together, all these characterization studies clearly reveal that the prepared Ir–W@Ir–WO_{3-x} nanoparticles possess a core–shell structure, as shown in Fig. 1i, in which the core is metallic Ir–W and the shell is amorphous Ir–WO_{3-x} with abundant oxygen vacancies.

The OER performance of Ir–WO_3 and Ir–W@Ir–WO_{3-x} grown on carbon cloth (CC) was evaluated in a 0.5 M H_2SO_4 aqueous electrolyte using a typical three-electrode cell, with the studied material, Ag/AgCl and a Pt plate as the working, reference and counter electrodes, respectively (details in Experimental section, ESI†). Commercial IrO_2 was also tested for comparison. The influence of iridium content on the OER performance was studied by controlling the addition of $H_2IrCl_6{\cdot}6H_2O$. Fig. S7 (ESI†) shows the XRD of Ir–W@Ir–WO_{3-x} with different Ir ratios. To precisely evaluate the effect of iridium content, we also compare the linear sweep voltammetry (LSV) curves normalized by the mass of the used Ir. Fig. S8 (ESI†) shows the OER activities with different iridium contents. With increase in iridium concentration, the catalytic activity of Ir–W@Ir–WO_{3-x} increases. However, further increasing the Ir ratio will result in the mass activity decay. Herein, the Ir ratio of 6.7 at% with maximum activity was adopted. Fig. 2a exhibits the LSV curves normalized by the geometrical area of the

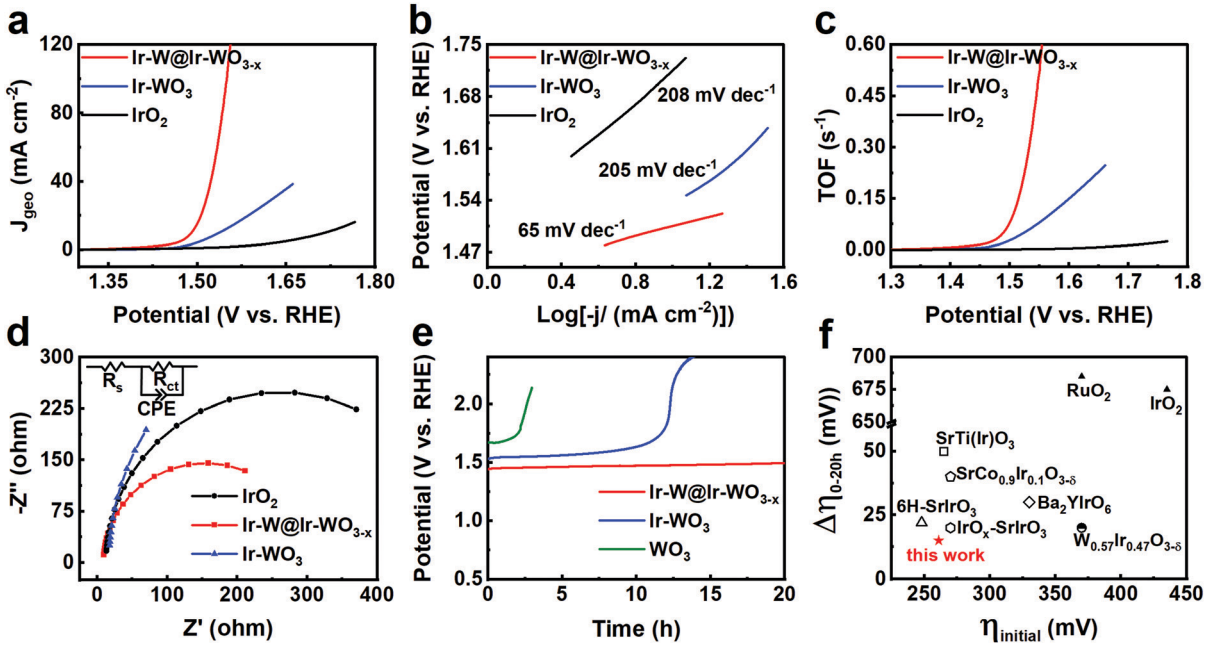

Fig. 2 (a) The LSV curves normalized by the geometric area and (b) the corresponding Tafel plots of Ir–W@Ir–WO_{3-x}, Ir–WO_3 and IrO_2 in 0.5 M H_2SO_4, respectively. (c) The potential-dependent TOF curves of Ir–W@Ir–WO_{3-x}, Ir–WO_3 and IrO_2. (d) Nyquist plots of Ir–W@Ir–WO_{3-x}, Ir–WO_3 and IrO_2 collected at the potential of 1.31 V *vs.* RHE. (e) Chronopotentiometric curves of Ir–W@Ir–WO_{3-x}, Ir–WO_3 and WO_3 recorded for 20 h at 10 mA cm^{-2}. (f) Performance comparison of Ir–W@Ir–WO_{3-x} with the ever-reported Ir-based catalysts under acidic conditions.

various working electrodes. The overpotential of Ir–W@Ir–WO_{3-x} toward OER catalysis at a current density of 10 mA cm^{-2} is only 261 mV, which is substantially lower than that of Ir–WO_3 (310 mV) and IrO_2 (486 mV). It also represents one of the best performances for OER catalysis under acidic conditions among the ever-reported Ir-based compounds (Fig. 2f).[15,16,21,22,25,35] Even at a high current density of 100 mA cm^{-2}, Ir–W@Ir–WO_{3-x} can still deliver an impressive overpotential of 318 mV. Besides, Ir–W@Ir–WO_{3-x} also has the lowest onset potential of around 1.4 V (potential required to reach 0.1 mA cm^{-2}), suggesting its extraordinary catalytic activity. Meanwhile, Tafel slope analysis (Fig. 2b) reveals that Ir–W@Ir–WO_{3-x} possesses a smaller Tafel slope of 65 mV dec^{-1}, indicating a faster kinetics in comparison with Ir–WO_3 (205 mV dec^{-1}) and IrO_2 (208 mV dec^{-1}).

Since the morphology has substantially changed, the electrochemical active surface area (ECSA) was further estimated to study the intrinsic catalytic activity (Fig. S9, ESI†). The double-layer capacitance (C_{dl}) of Ir–W@Ir–WO_{3-x} NPs was calculated to be 36 mF cm^{-2}, which is slightly larger than that of Ir–WO_3 NWs (27 mF cm^{-2}). Moreover, the BET measurements were also conducted, as shown in Fig. S10 (ESI†), Ir–W@Ir–WO_{3-x} NPs delivered a more larger surface area of 208.8 m^2 g^{-1} than that of Ir–WO_3 NWs (127.8 m^2 g^{-1}). To eliminate the effects of surface area variation on OER activity and unravel the intrinsic per-site activity, the turn-over frequency (TOF) was estimated based on the ECSA data (details for the TOF calculation in Experimental section, ESI†). Fig. 2c reveals that the TOF values of Ir–W@Ir–WO_{3-x} are extraordinarily larger than the values of Ir–WO_3 NWs at the studied potential range, suggesting that the per-site activity has been substantially increased. At a potential of 1.5 V, the TOF value of Ir–W@Ir–WO_{3-x} is 2.94 times larger than the value of the Ir–WO_3. Considering that Ir is an expensive noble metal, the catalytic performance was further normalized by the mass of the used Ir. Fig. S11 (ESI†) shows the mass normalized LSV curves. Impressively, the mass activity of Ir–W@Ir–WO_{3-x} NPs is about 3.5 and 18.7 times higher than that of Ir–WO_3 NWs and commercial IrO_2, respectively, at a potential of 1.5 V *vs.* RHE. The prominent intrinsic mass activity toward OER catalysis indicates an enhanced atomic utilization and a decreased catalyst cost. Furthermore, electrochemical impedance spectroscopy (EIS) was conducted to probe the charge transfer kinetics at the interface between the electrode and electrolyte (Fig. 2d). Generally, a small charge transfer resistance (R_{ct}) indicates fast interfacial charge transfer kinetics. The R_{ct} values of the studied three samples follows the decreased order of Ir–WO_3 NWs > IrO_2 NPs > Ir–W@Ir–WO_{3-x} NPs, indicating that Ir–W@Ir–WO_{3-x} NPs have the best catalytic feature in interfacial charge transfer.

Stability is another vital parameter of catalytic performance, especially for acidic OER. Therefore, chronopotentiometry (CP) was carried out for stability study. Fig. 2e exhibits the CP curves of Ir–W@Ir–WO_{3-x}, Ir–WO_3 and WO_3 at a constant current density of 10 mA cm^{-2}. WO_3 and Ir–WO_3 start to deactivate after 1.5 h and 10 h, respectively. Impressively, Ir–W@Ir–WO_{3-x} can well maintain the high catalytic activity for a continuous 20 h test with merely 3.5% voltage increase. Besides, the LSV curves (Fig. S12, ESI†) of Ir–W@Ir–WO_{3-x} after a 20 h test show that the overpotential decay is only 13 mV after 20 h, demonstrating the robust catalytic stability toward acidic OER. Fig. 2f and Table S1 (ESI†) compare the activity (overpotential at 10 mA cm^{-2})

and the stability (overpotential increasing in 20 h) of Ir–W@Ir–WO_{3-x} with the ever-reported acidic OER catalysts.[15,16,21,22,25,35] Apparently, Ir–W@Ir–WO_{3-x} outperforms most of the reported catalysts not only in activity, but also in stability.

To probe the stability of the structures and electronic states, SEM, XRD and XPS characterization studies on the catalysts were performed after stability test. The SEM images indicate that the particle morphology of Ir–W@Ir–WO_{3-x} can be well maintained after the stability test (Fig. S13, ESI†). Meanwhile, structural phase analysis by XRD (Fig. 3a) finds that the cubic phase of tungsten is also retained, indicating that the whole crystal structure is robust during the acidic OER catalysis. By comparing the XPS spectra of Ir 4f and W 4f spectra before and after OER catalysis, it was found that the ratios of Ir^{4+} and W^{6+} are increased after OER stability test, which is probably attributed to the partial oxidation of Ir^{3+} and W^{5+} (Fig. 3b and c). All these results suggest that the whole structures of Ir–W@Ir–WO_{3-x} can be well maintained during the acidic OER catalysis.

Given that peroxide intermediate species generated during OER catalysis are the key factors that affect the stability of tungsten-based catalysts,[36,37,39,40,47] the concentration of peroxide products was further detected and the dissolution of W and Ir was monitored in the electrolyte. The generation of peroxide products can be detected using a color developing agent (CPA) (details in supplementary method, ESI†) by ultraviolet-visible (UV-vis) adsorption spectroscopy.[48] Before testing, a standard calibration curve (the absorption intensity at 257 nm *versus* the concentration of H_2O_2, Fig. S14, ESI†) was performed. Fig. 3d shows the UV-vis spectra of the blank electrolyte solution and the solution after catalytic tests for 30 min at a current density of 10 mA cm^{-2} with WO_3, Ir–WO_3, and Ir–W@Ir–WO_{3-x} catalysts, respectively. Apparently, the absorption intensity of the solution with the Ir–W@Ir–WO_{3-x} catalysts is almost overlapped with that of the blank solution, suggesting that the generation of peroxide intermediates is negligible due to Ir induced low selectivity toward H_2O_2 production. On comparison, the obvious absorption intensities of pristine WO_3 and Ir–WO_3 indicate that the peroxide species cannot be well suppressed, which could be the reason for the unstable catalytic performance. Quantitatively, the concentration of the generated peroxide species during OER catalysis was estimated using the standard calibration curve (Fig. S14, ESI†). Within the 30 min test, the contents of peroxide species in the electrolyte using WO_3, Ir–WO_3 and Ir–W@Ir–WO_{3-x} as the OER catalysts are 3.99, 0.013 and 0 μg mL^{-1}, respectively (Fig. 3e). This indicates that Ir–W@Ir–WO_{3-x} can effectively prevent the production of peroxide species. Besides, the ICP-AES was further employed to monitor metal dissolution during OER catalysis. As shown in Fig. 3f, the dissolution of iridium and tungsten is very limited for the Ir–W@Ir–WO_{3-x} catalyst, which is consistent with the peroxide species generation results. Taken together, structural analysis after the OER test and dissolution analysis reveal that controlling the generation of the peroxide intermediate is the key to achieving stable OER catalysis for tungsten-based catalysts.

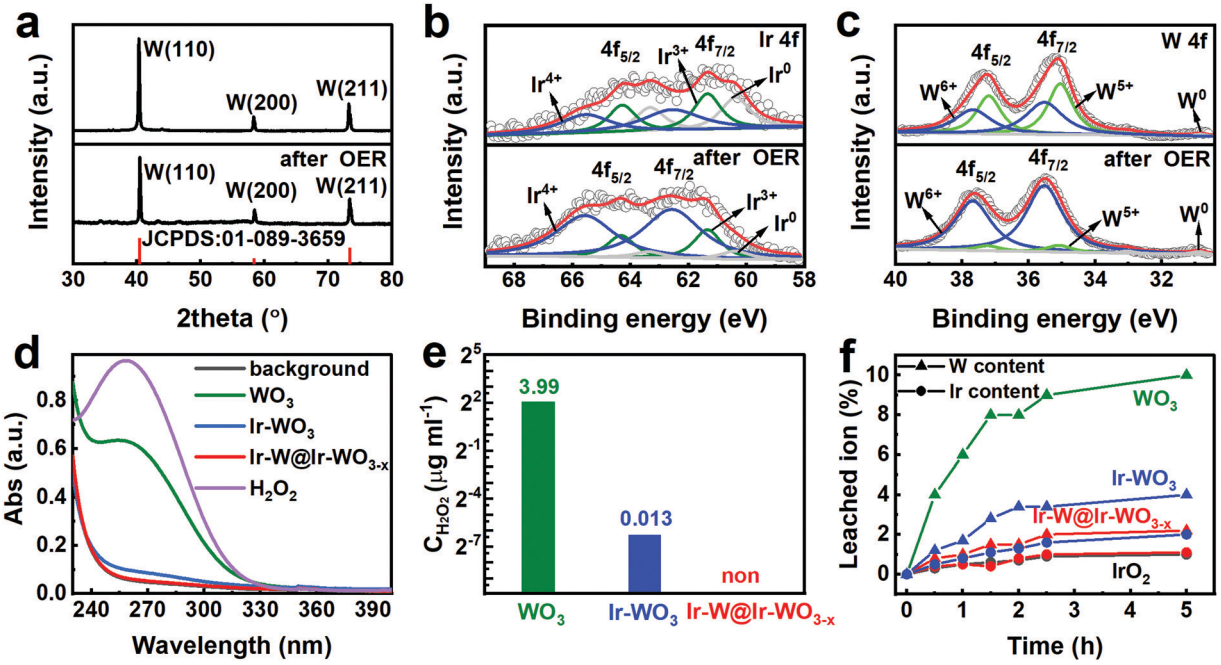

Fig. 3 (a) Comparison of XRD patterns of Ir–W@Ir–WO_{3-x} before and after the stability test, (b) XPS core-level spectra of Ir 4f and (c) W 4f for Ir–W@Ir–WO_{3-x} before and after stability test. (d) UV-visible absorption spectrum of the electrolyte solution after 30 min CP test with the Ir–W@Ir–WO_{3-x}, Ir–WO_3 and WO_3 as the working electrodes, respectively, while the background electrolyte and the electrolyte with the addition of H_2O_2 (6.02 μg mL^{-1}) are used as reference. (e) The estimated H_2O_2 concentrations based on the UV-vis spectra in (d). (f) ICP-AES analysis to estimate the leached W and Ir weight percentage of Ir–W@Ir–WO_{3-x}, Ir–WO_3, IrO_2, and WO_3 under different reaction times.

To reveal the underlying mechanism at the atomic level for the excellent OER activity and dissolution resistance of the Ir–W@Ir–WO_{3-x} catalyst, density functional theory calculations were performed on the Ir–W@Ir–WO_{3-x}(110), Ir–WO_3(001) and WO_3(001) surfaces. The model construction is according to the experimental structural characterization. In particular, the Ir–W@Ir–WO_{3-x} catalyst contains five possible surface configurations including W@Ir–WO_3(110), W@Ir–WO_3–O_v(110), Ir_{sur}–W@Ir–WO_3(110), Ir_{sur}–W@Ir–WO_3–O_v(110) and Ir_{sub}–W@Ir–WO_3–O_v(110) (the details are shown in Fig. S15, ESI†). Subsequently, the catalytic activities were explored in term of the OER overpotential based on the four-step OER pathway,[25,49] which proceeds through OH*, O*, and OOH* intermediates. Firstly, the free energies of OH*, O* and OOH* were calculated on the WO_3(001), Ir–WO_3(001) and Ir–W@Ir–WO_{3-x} surfaces, respectively. The results indicate that the free energy of OOH* is linearly related to that of OH* on the WO_3(001), Ir–WO_3(001) and Ir–W@Ir–WO_{3-x} surfaces, following the equation $\Delta G_{OOH^*} = 0.91\Delta G_{OH^*} + 3.2 \pm 0.2$ (Fig. 4a), which supports the hypothesis of four-step OER mechanism and is in good agreement with previous work.[25,49]

The overpotential (η) was obtained according to the four-step OER mechanism (Fig. S16–S22, ESI†). For the Ir–W@Ir–WO_{3-x} catalysts, the minimum overpotential is 0.49 V over the Ir_{sub}–W@Ir–WO_3–O_v(110) surface, which is lower than that on W@Ir–WO_3(110) (0.87 V), W@Ir–WO_3–O_v(110) (0.56 V), Ir_{sur}–W@Ir–WO_3(110) (0.64 V), and Ir_{sur}–W@Ir–WO_3–O_v(110) (0.62 V) surfaces, suggesting that Ir_{sub}–W@Ir–WO_3–O_v(110) is the best structural configuration of Ir–W@Ir–WO_{3-x} for OER catalysis. In the following analysis, the structural model of Ir_{sub}–W@Ir–WO_3–O_v(110) is used as a typical catalytic surface for Ir–W@Ir–WO_{3-x}. More importantly, the calculated η over Ir_{sub}–W@Ir–WO_3–O_v(110) surface is more favorable than Ir–WO_3(001) and WO_3(001) surfaces with η values of 0.58 and 1.05 V, respectively, which are the reason why Ir–W@Ir–WO_{3-x} display better catalytic activity than WO_3 and Ir–WO_{3-x}.

Since pursuing the volcano peak of the OER catalysts is of great significance for catalytic studies, the calculated η with respect to the free energy of the O* and OH* intermediates is further presented using a 2D volcano plot (Fig. 4b). Based on the 2D volcano plot and the Gibbs free energy diagrams (Fig. S16–S22, ESI†), a large ΔG_{O^*}–ΔG_{OH^*} value impedes the adsorption of OH* and the subsequent dehydrogenation to form O*, while a small ΔG_{O^*}–ΔG_{OH^*} value is detrimental for the formation of the OOH* intermediate. The Gibbs free energy diagrams reveal that the potential-determining step is primarily related to the second step ($OH^* + H_2O \rightarrow O^* + H_2O + H^+ + e^-$) or the third step ($O^* + H_2O \rightarrow OOH^* + H^+ + e^-$) on the Ir–W@Ir–$WO_{3-x}$, Ir–$WO_3$ and WO_3 catalysts. Therefore, the adsorption behavior of O was further analyzed.[30] The charge density difference (Fig. 4c) shows that the charge interaction between O and Ir in Ir_{sub}–W@Ir–WO_3–O_v(110) surface is stronger than the W–O interaction in WO_3(001) but weaker than the Ir–O interaction in Ir–WO_3(001), which leads to a moderate adsorption free energy toward O on the Ir_{sub}–W@Ir–WO_3–O_v(110) surface. The moderate adsorption capability could endow

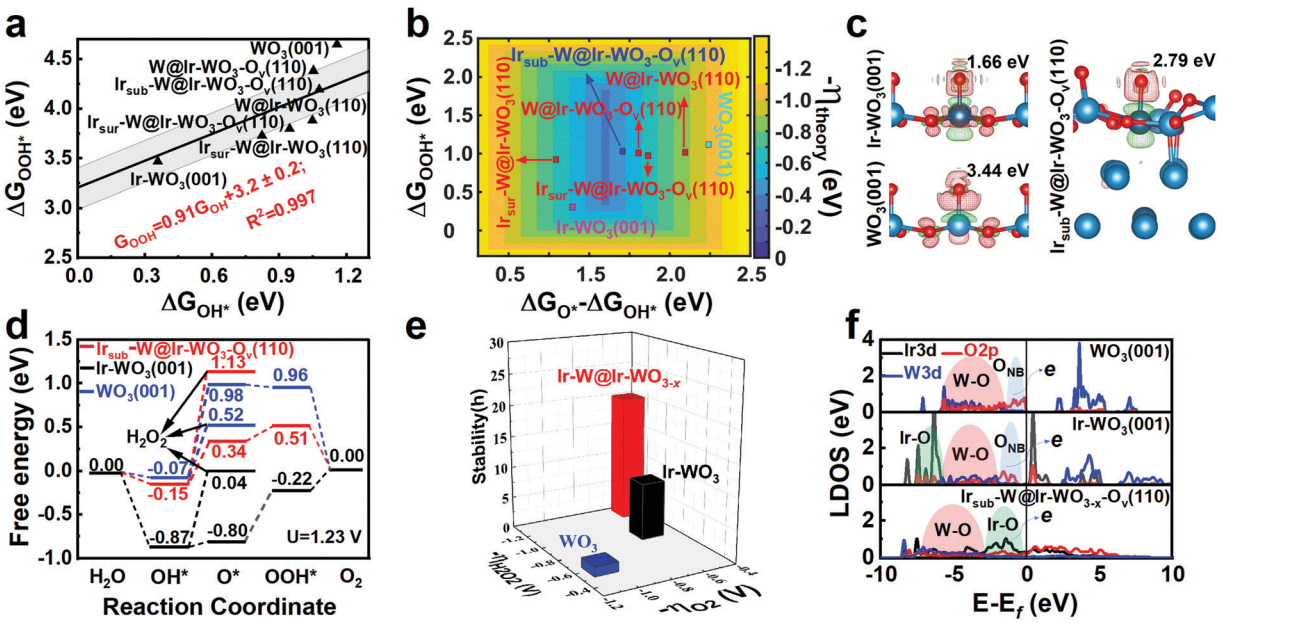

Fig. 4 (a) The linear scaling relationship between ΔG_{OOH^*} and ΔG_{OH^*} for the seven kinds of surfaces listed in Fig. S16–S22 (ESI†). (b) Volcano plots of the theoretical overpotential towards G_{OH^*} and $G_{O^*-OOH^*}$. (c) Calculated charge density differences and adsorption free energy ($\Delta\rho = \rho(O/slab) - \rho(slab) - \rho(O)$) of oxygen on WO_3(001), Ir–WO_3(001) and Ir_{sub}–W@Ir–WO_3–O_v(110), respectively; the value of absolute isosurface is 0.008 e Å^{-3}. (d) Standard free energy diagram for the OER and H_2O_2 at equilibrium potential for oxygen evolution (U = 1.23 V) over WO_3(001), Ir–WO_3(001) and Ir_{sub}–W@Ir–WO_3–O_v(110), respectively. (e) Comparison of experimental and theoretical data for the OER stability. (f) Local DOS of WO_3(001), Ir–WO_3(001) and Ir_{sub}–W@Ir–WO_3–O_v(110), respectively, with respect to the Fermi level.

Ir_{sub}–W@Ir–WO_3–O_v(110) with superior catalytic activity by balancing the potential-determining steps, which is well consistent with the experimental observation.

Considering that the generation of hydroperoxide is responsible for the stability of the catalysts, the formation of H_2O_2 on the WO_3(001), Ir–WO_3(001) and Ir_{sub}–W@Ir–WO_3–O_v(110) surfaces was s-ystematically analyzed.[40] Fig. 4d exhibits the energy barrier for H_2O_2 formation on the Ir_{sub}–W@Ir–WO_3–O_v(110), Ir–WO_3(001) and WO_3(001) surfaces, in which Ir_{sub}–W@Ir–WO_3–O_v(110) has the largest energy barrier. And the energy barrier of H_2O_2 formation follows the order of WO_3(001) < Ir–WO_3(001) < Ir_{sub}–W@Ir–WO_3–O_v(110), which is contrary to the oxygen formation activity. The correlation between the experimental results and the theoretically calculated η was further plotted (Fig. 4e). This indicates that the lowest oxygen evolution reaction overpotential and the highest peroxide formation energy barrier enables Ir–W@Ir–WO_{3-x} to be the most active and stable catalyst toward OER catalysis. In order to uncover the modulation essence of the electronic structure on stability, the local density of states (LDOS) analysis is carried out on the Ir_{sub}–W@Ir–WO_3–O_v(110), Ir–WO_3(001) and WO_3(001) surfaces. As shown in Fig. 4f, the introduction of Ir in Ir–WO_3 can effectively eliminate almost all of the unoccupied portions of the non-bonding state oxygen (O_{NB}) around E_f, leading to both O_{NB} and W–O overlap far away from the E_f level relative to WO_3 and enhancing the durability of Ir–WO_3 catalyst from the corrosion of hydroperoxide.

Conclusions

In summary, we have demonstrated that the rational modulation of surface adsorption toward oxygen-containing intermediates on tungsten-based catalysts can enhance both catalytic activity and stability for acidic OER catalysis. The constructed Ir–W@Ir–WO_{3-x} core–shell nanoparticles achieve a low overpotential of 261 mV at 10 mA cm^{-2} and excellent stability with merely 3.5% potential increase for 20 h chronopotentiometric test, which outperform most of the ever-reported acidic OER catalysts. Spectroscopic analysis indicates that the suppression of hydroperoxide formation is responsible for the excellent stability of the catalyst. DFT calculations further uncover that the moderate adsorption strength of oxygen-containing intermediates on Ir–W@Ir–WO_{3-x} not only accelerates the oxygen evolution reaction, but also restrains the formation of hydroperoxide, which thus enable the superior catalytic activity and stability for acidic OER catalysis. This work could provide significant insights for the design of highly efficient and stable OER catalysts and beyond.

Author contributions

G. M. W. and S. W. N. designed and supervised the project. Z. L. and C. W. conducted the project and contributed equally to this work. J. Y. and Y. Y. F. conducted XPS measurements. Y. P. Z., Y. S. W., D. S., D. N., A. M., X. M. L., Z. B. P. and J. Y. C. performed XRD, SEM and TEM characterization. C. W., X. B. H. and S. W. N. provided the DFT calculation. G. M. W., S. W. N. and Z. L. wrote and revised the manuscript, and all the authors discussed the results and commented on the manuscript.

Conflicts of interest

There are no conflicts of interest to declare.

Acknowledgements

The authors thank the financial support of the Natural Science Fund of China (21771169), the National Key Research and Development Program of China (2017YFA0206703), the Fundamental Research Funds for the Central Universities (WK2060000016), and the Collaborative Innovation program of Hefei Science Center, CAS. We also thank the Hefei National Synchrotron Radiation Laboratory (BL10B, NSRL) for XPS characterization. The numerical calculations in this article were performed using the supercomputing system in the Supercomputing Center of University of Science and Technology of China.

References

1 C. Choi, S. Kwon, T. Cheng, M. Xu, P. Tieu, C. Lee, J. Cai, H. M. Lee, X. Pan, X. Duan, W. A. Goddard and Y. Huang, Highly active and stable stepped Cu surface for enhanced electrochemical CO_2 reduction to C_2H_4, *Nat. Catal.*, 2020, **3**, 804–812.

2 H. Fei, J. Dong, D. Chen, T. Hu, X. Duan, I. Shakir, Y. Huang and X. Duan, Single atom electrocatalysts supported on graphene or graphene-like carbons, *Chem. Soc. Rev.*, 2019, **48**, 5207–5241.

3 Z. W. Seh, J. Kibsgaard, C. F. Dickens, I. Chorkendorff, J. K. Norskov and T. F. Jaramillo, Combining theory and experiment in electrocatalysis: Insights into materials design, *Science*, 2017, **355**, 146.

4 J. Chen, P. Cui, G. Zhao, K. Rui, M. Lao, Y. Chen, X. Zheng, Y. Jiang, H. Pan, S. X. Dou and W. Sun, Low-coordinate iridium oxide confined on graphitic carbon nitride for highly efficient oxygen evolution, *Angew. Chem., Int. Ed.*, 2019, **58**, 12540–12544.

5 T. Kou, S. Wang, J. L. Hauser, M. Chen, S. R. J. Oliver, Y. Ye, J. Guo and Y. Li, Foam-supported Fe-doped β-$Ni(OH)_2$ nanosheets show ultralow overpotential for oxygen evolution reaction, *ACS Energy Lett.*, 2019, **4**, 622–628.

6 T. Kou, S. Wang and Y. Li, Perspective on high-rate alkaline water splitting, *ACS Mater. Lett.*, 2021, **3**, 224–234.

7 C. Liang, P. Zou, A. Nairan, Y. Zhang, J. Liu, K. Liu, S. Hu, F. Kang, H. J. Fan and C. Yang, Exceptional performance of hierarchical Ni–Fe oxyhydroxide@NiFe alloy nanowire array electrocatalysts for large current density water splitting, *Energy Environ. Sci.*, 2020, **13**, 86–95.

8 P. Liu, B. Chen, C. Liang, W. Yao, Y. Cui, S. Hu, P. Zou, H. Zhang, H. J. Fan and C. Yang, Tip-enhanced electric field: a new mechanism promoting mass transfer in oxygen evolution reactions, *Adv. Mater.*, 2021, **33**, 2007377.

9 L. Yang, R. Liu and L. Jiao, Electronic redistribution: construction and modulation of interface engineering on CoP for enhancing overall water splitting, *Adv. Funct. Mater.*, 2020, **30**, 1909618.

10 J. L. Guan, C. F. Li, J. W. Zhao, Y. Z. Yang, W. Zhou, Y. Wang and G. R. Li, FeOOH-enhanced bifunctionality in Ni_3N nanotube arrays for water splitting, *Appl. Catal., B*, 2020, **269**, 118600.

11 B. Zhang, L. Wang, Z. Cao, S. M. Kozlov, F. P. García de Arquer, C. T. Dinh, J. Li, Z. Wang, X. Zheng, L. Zhang, Y. Wen, O. Voznyy, R. Comin, P. De Luna, T. Regier, W. Bi, E. E. Alp, C.-W. Pao, L. Zheng, Y. Hu, Y. Ji, Y. Li, Y. Zhang, L. Cavallo, H. Peng and E. H. Sargent, High-valence metals improve oxygen evolution reaction performance by modulating 3d metal oxidation cycle energetics, *Nat. Catal.*, 2020, **3**, 985–992.

12 G. Zhao, P. Li, N. Cheng, S. X. Dou and W. Sun, An Ir/$Ni(OH)_2$ heterostructured electrocatalyst for the oxygen evolution reaction: breaking the scaling relation, stabilizing iridium(V), and beyond, *Adv. Mater.*, 2020, **32**, 2000872.

13 J. Xing, Y. Li, S. Guo, T. Jin, H. Li, Y. Wang and L. Jiao, Molybdenum carbide in-situ embedded into carbon nanosheets as efficient bifunctional electrocatalysts for overall water splitting, *Electrochim. Acta*, 2019, **298**, 305–312.

14 Z. D. Huang, C. Feng, J. P. Sun, B. Xu, T. X. Huang, X. K. Wang, F. N. Dai and D. F. Sun, Ultrathin Metal–Organic Framework Nanosheets-Derived Yolk–Shell $Ni_{0.85}Se$@NC with Rich Se-Vacancies for Enhanced Water Electrolysis, *CCS Chem.*, 2020, **2**, 2696–2711.

15 J. Lei, M. Zeng and L. Fu, Two-dimensional Metal-Organic Frameworks as Electrocatalysts for Oxygen Evolution Reaction, *Chem. Res. Chin. Univ.*, 2020, **36**, 504–510.

16 Y. Sun, L. Yuan, Z. Liu, Q. Wang, K. Huang and S. Feng, Optimization of oxygen evolution dynamics on RuO_2 via controlling of spontaneous dissociation equilibrium, *Mater. Chem. Front.*, 2019, **3**, 1779–1785.

17 H. Wang, J. Qi, N. Yang, W. Cui, J. Wang, Q. Li, Q. Zhang, X. Yu, L. Gu, J. Li, R. Yu, K. Huang, S. Song, S. Feng and D. Wang, Dual-Defects Adjusted Crystal-Field Splitting of $LaCo_{1-x}Ni_xO_{3-\delta}$ Hollow Multishelled Structures for Efficient Oxygen Evolution, *Angew. Chem., Int. Ed.*, 2020, **59**, 19691–19695.

18 C. Yang, H. F. Wang and Q. Xu, Recent Advances in Two-dimensional Materials for Electrochemical Energy Storage and Conversion, *Chem. Res. Chin. Univ.*, 2020, **36**, 10–23.

19 Y. Zhang, Z. Zeng and D. Ho, Mn dopant induced high-valence Ni^{3+} sites and oxygen vacancies for enhanced water oxidation, *Mater. Chem. Front.*, 2020, **4**, 1993–1999.

20 Y. Zhao, N. Yang, H. Yao, D. Liu, L. Song, J. Zhu, S. Li, L. Gu, K. Lin and D. Wang, Stereodefined Codoping of sp-N and S Atoms in Few-Layer Graphdiyne for Oxygen Evolution Reaction, *J. Am. Chem. Soc.*, 2019, **141**, 7240–7244.

21 Y. G. Zhou, Y. Kang and J. Huang, Fluidized Electrocatalysis, *CCS Chem.*, 2019, **2**, 31–41.

22 D. He, X. Song, W. Li, C. Tang, J. Liu, Z. Ke, C. Jiang and X. Xiao, Active electron density modulation of Co_3O_4-based catalysts enhances their oxygen evolution performance, *Angew. Chem., Int. Ed.*, 2020, **59**, 6929–6935.

23 O. Diaz-Morales, S. Raaijman, R. Kortlever, P. J. Kooyman, T. Wezendonk, J. Gascon, W. T. Fu and M. T. Koper, Iridium-based double perovskites for efficient water oxidation in acid media, *Nat. Commun.*, 2016, **7**, 12363.

24 L. C. Seitz, C. F. Dickens, K. Nishio, Y. Hikita, J. Montoya, A. Doyle, C. Kirk, A. Vojvodic, H. Y. Hwang, J. K. Norskov and T. F. Jaramillo, A highly active and stable $IrO_x/SrIrO_3$ catalyst for the oxygen evolution reaction, *Science*, 2016, **353**, 1011–1014.

25 Y. Yao, S. Hu, W. Chen, Z. Q. Huang, W. Wei, T. Yao, R. Liu, K. Zang, X. Wang, G. Wu, W. Yuan, T. Yuan, B. Zhu, W. Liu, Z. Li, D. He, Z. Xue, Y. Wang, X. Zheng, J. Dong, C. R. Chang, Y. Chen, X. Hong, J. Luo, S. Wei, W. X. Li, P. Strasser, Y. Wu and Y. Li, Engineering the electronic structure of single atom Ru sites via compressive strain boosts acidic water oxidation electrocatalysis, *Nat. Catal.*, 2019, **2**, 304–313.

26 J. Wu, M. Liu, K. Chatterjee, K. P. Hackenberg, J. Shen, X. Zou, Y. Yan, J. Gu, Y. Yang, J. Lou and P. M. Ajayan, Exfoliated 2D transition metal disulfides for enhanced electrocatalysis of oxygen evolution reaction in acidic medium, *Adv. Mater. Interfaces*, 2016, **3**, 1500669.

27 H. Chen, L. Shi, X. Liang, L. Wang, T. Asefa and X. Zou, Optimization of active sites via crystal phase, composition, and morphology for efficient low-iridium oxygen evolution catalysts, *Angew. Chem., Int. Ed.*, 2020, **59**, 19654–19658.

28 S. Moller, S. Barwe, J. Masa, D. Wintrich, S. Seisel, H. Baltruschat and W. Schuhmann, Online monitoring of electrochemical carbon corrosion in alkaline electrolytes by differential electrochemical mass spectrometry, *Angew. Chem., Int. Ed.*, 2020, **59**, 1585–1589.

29 Y. Chen, H. Li, J. Wang, Y. Du, S. Xi, Y. Sun, M. Sherburne, J. W. Ager, A. C. Fisher and Z. J. Xu, Exceptionally active iridium evolved from a pseudo-cubic perovskite for oxygen evolution in acid, *Nat. Commun.*, 2019, **10**, 572.

30 X. Liang, L. Shi, Y. Liu, H. Chen, R. Si, W. Yan, Q. Zhang, G. D. Li, L. Yang and X. Zou, Activating Inert, Nonprecious perovskites with iridium dopants for efficient oxygen evolution reaction under acidic conditions, *Angew. Chem., Int. Ed.*, 2019, **58**, 7631–7635.

31 H. N. Nong, H. S. Oh, T. Reier, E. Willinger, M. G. Willinger, V. Petkov, D. Teschner and P. Strasser, Oxide-supported IrNiO(x) core-shell particles as efficient, cost-effective, and stable catalysts for electrochemical water splitting, *Angew. Chem., Int. Ed.*, 2015, **54**, 2975–2979.

32 H. N. Nong, T. Reier, H. S. Oh, M. Gliech, P. Paciok, T. H. T. Vu, D. Teschner, M. Heggen, V. Petkov, R. Schlögl, T. Jones and P. Strasser, A unique oxygen ligand environment facilitates water oxidation in hole-doped $IrNiO_x$ core–shell electrocatalysts, *Nat. Catal.*, 2018, **1**, 841–851.

33 L. Yang, G. Yu, X. Ai, W. Yan, H. Duan, W. Chen, X. Li, T. Wang, C. Zhang, X. Huang, J. S. Chen and X. Zou, Efficient oxygen evolution electrocatalysis in acid by a perovskite with face-sharing IrO6 octahedral dimers, *Nat. Commun.*, 2018, **9**, 5236.

34 M. Etzi Coller Pascuzzi, J. P. Hofmann and E. J. M. Hensen, Promoting oxygen evolution of IrO_2 in acid electrolyte by Mn, *Electrochim. Acta*, 2021, **366**, 137448.

35 W. Gou, M. Zhang, Y. Zou, X. Zhou and Y. Qu, Iridium-Chromium Oxide Nanowires as Highly Performed OER Catalysts in Acidic Media, *ChemCatChem*, 2019, **11**, 6008–6014.

36 G. Wang, Y. Ling, H. Wang, X. Yang, C. Wang, J. Z. Zhang and Y. Li, Hydrogen-treated WO_3 nanoflakes show enhanced photostability, *Energy Environ. Sci.*, 2012, **5**, 6180–6187.

37 V. Chakrapani, J. Thangala and M. K. Sunkara, WO_3 and W_2N nanowire arrays for photoelectrochemical hydrogen production, *J. Hydrogen Energy*, 2009, **34**, 9050–9059.

38 P. C. Murau, Dissolution of Tungsten by Hydrogen Peroxide, *Anal. Chem.*, 1961, **33**, 1125–1126.

39 Y. Wang, W. Tian, C. Chen, W. Xu and L. Li, Tungsten trioxide nanostructures for photoelectrochemical water splitting: material engineering and charge carrier dynamic manipulation, *Adv. Funct. Mater.*, 2019, **29**, 1809036.

40 V. Viswanathan, H. A. Hansen and J. K. Norskov, Selective electrochemical generation of hydrogen peroxide from water oxidation, *J. Phys. Chem. Lett.*, 2015, **6**, 4224–4228.

41 S. Rajagopal, H.-M. Lee, K. Lee and C.-K. Kim, Hydrothermal synthesis of one-dimensional tungsten oxide nanostructures using cobalt ammonium sulfate as a structure-directing agent, *Korean J. Chem. Eng.*, 2013, **30**, 1833–1835.

42 H. R. Zhang and O. A. Ojo, TEM analysis of Cr–Mo–W–B phase in a DS nickel based superalloy, *J. Mater. Sci.*, 2008, **43**, 6024–6028.

43 S. Kumari, B. P. Ajayi, B. Kumar, J. B. Jasinski, M. K. Sunkara and J. M. Spurgeon, A low-noble-metal $W_{1-x}Ir_xO_{3-\delta}$ water oxidation electrocatalyst for acidic media via rapid plasma synthesis, *Energy Environ. Sci.*, 2017, **10**, 2432–2440.

44 J. Shan, C. Guo, Y. Zhu, S. Chen, L. Song, M. Jaroniec, Y. Zheng and S. Qiao, Charge-redistribution-enhanced nanocrystalline Ru@IrO_x electrocatalysts for oxygen evolution in acidic media, *Chem*, 2019, **5**, 445–459.

45 M. Seifollahi Bazarjani, M. Hojamberdiev, K. Morita, G. Zhu, G. Cherkashinin, C. Fasel, T. Herrmann, H. Breitzke, A. Gurlo and R. Riedel, Visible light photocatalysis with c-WO_{3-x}/WO_3xH_2O nanoheterostructures in situ formed in mesoporous polycarbosilane-siloxane polymer, *J. Am. Chem. Soc.*, 2013, **135**, 4467–4475.

46 M. G. Kim, H. S. Kim, Y.-G. Ha, J. He, M. G. Kanatzidis, A. Facchetti and T. J. Marks, High-performance solution-processed amorphous zinc–indium–tin oxide thin-film transistors, *J. Am. Chem. Soc.*, 2010, **132**, 10352–10364.

47 W. Li, J. Li, X. Wang, J. Ma and Q. Chen, Photoelectrochemical and physical properties of WO_3 films obtained by the polymeric precursor method, *J. Hydrogen Energy*, 2010, **35**, 13137–13145.

48 G. Telep and D. F. Boltz, Ultraviolet Spectrophotometric determination of cobalt with peroxide and bicarbonate, *Anal. Chem.*, 1952, **24**, 945–947.

49 J. Rossmeisl, Z. W. Qu, H. Zhu, G. J. Kroes and J. K. Nørskov, Electrolysis of water on oxide surfaces, *J. Electroanal. Chem.*, 2007, **607**, 83–89.

